



Comparison of aerosol measurement systems during the 2016 airborne ARISTO campaign

John Ortega, Jefferson R. Snider, James N. Smith & J. Michael Reeves

To cite this article: John Ortega, Jefferson R. Snider, James N. Smith & J. Michael Reeves (2019) Comparison of aerosol measurement systems during the 2016 airborne ARISTO campaign, *Aerosol Science and Technology*, 53:8, 871-885, DOI: [10.1080/02786826.2019.1610554](https://doi.org/10.1080/02786826.2019.1610554)

To link to this article: <https://doi.org/10.1080/02786826.2019.1610554>

 View supplementary material 

 Accepted author version posted online: 25 Apr 2019.
Published online: 16 May 2019.

 Submit your article to this journal 

 Article views: 157

 View related articles 

 View Crossmark data 
CrossMark



Comparison of aerosol measurement systems during the 2016 airborne ARISTO campaign

John Ortega^a, Jefferson R. Snider^b, James N. Smith^c, and J. Michael Reeves^d

^aNational Center for Atmospheric Research, Atmospheric Chemistry Observations and Modeling Laboratory, Boulder, Colorado, USA;

^bDepartment of Atmospheric Science, University of Wyoming, Laramie, Wyoming, USA; ^cDepartment of Chemistry, University of California, Irvine, Irvine, California, USA; ^dNational Center for Atmospheric Research, Earth Observing Laboratory, Research Aviation Facility, Broomfield, Colorado, USA

ABSTRACT

Several different types of measurements of particle size and concentration were compared during the 2016 Airborne Research Instrumentation Testing Opportunity (ARISTO) campaign. The scanning mobility particle sizer (SMPS) measured number-size distributions for mobility diameters between ~20–350 and ~8–110 nm, depending on the mobility analyzer chosen. Also included were two stand-alone condensation particle counters (CPC) for determining size-integrated particle concentrations. A wing-mounted and a rack-mounted Ultra-High Sensitivity Aerosol Spectrometer (UHSAS) were used to measure size distributions between 60 and 1000 nm. Lastly, two different sampling inlets were used to investigate performance and observe any systematic biases. Most sampling occurred during cloud-free summer conditions in the western United States. Number concentrations from the two CPCs typically agreed within 12% once the flows in the ultrafine particle counter were corrected as a function of pressure. As expected, the size-integrated number concentrations from the SMPS and UHSAS were generally less than those of the CPCs, as the former cover only part of the total range of particle sizes measured by the CPCs. Integrated number concentrations from the wing-mounted and rack-mounted UHSAS generally agreed within 20% for all diameter ranges analyzed. The overlap region between the SMPS and the UHSAS showed reasonable agreement of ±20%. Some of the uncertainty regarding these measurement comparisons originates from a variety of factors, including sampling frequency, particle refractive index, differences between physical and mobility diameters, and counting efficiency uncertainties in the UHSAS optical cavity, especially for the smallest diameters (60–100 nm).

ARTICLE HISTORY

Received 17 August 2018

Accepted 4 April 2019

EDITOR

Jingkun Jiang

1. Introduction

Aerosol particles have long been recognized for their impact on human health, visibility, and climate (Fan et al. 2016; Malm 2016; Shiraiwa et al. 2017). While these topics remain both scientifically and socially relevant, contemporary investigations are focused on fundamental chemical aspects; e.g., new particle formation, particle growth, gas-particle partitioning (Seinfeld and Pandis 1998). Assisting these investigations are techniques that measure aerosol mass, surface area, number concentration, and other chemical and physical properties of aerosol particles (McMurtry 2000; Kulkarni et al. 2011). These particles have a wide range of properties including size, shape, composition, phase (liquid, solid, mixed), location in the

atmosphere, and chemical processes leading to both particle growth and mass loss. Aerosol particles undergo chemical reactions, growth, and coagulation, and they interact with both clouds and existing aerosol. Because of these interactions, aerosol properties vary significantly in space and time. Given this variability, it is important to have the ability to measure from mobile platforms such as balloons, aircraft, and autonomous aerial vehicles. The NSF-sponsored program Airborne Research Instrumentation Testing Opportunity (ARISTO) is a program administered by the Earth Observing Laboratory at the National Center for Atmospheric Research (NCAR) that accepts proposals to test certain instruments, inlets and support other scientific objectives in the pursuit

CONTACT John Ortega ortega.john@gmail.com National Center for Atmospheric Research, Atmospheric Chemistry Observations and Modeling Laboratory, PO Box 3000, Boulder, CO 80301, USA.

All data from the instruments used in this study are archived and freely available (Ortega et al. 2019).

Color versions of one or more of the figures in the article can be found online at www.tandfonline.com/uast.

Supplemental data for this article is available online at <https://doi.org/10.1080/02786826.2019.1610554>.

© 2019 American Association for Aerosol Research

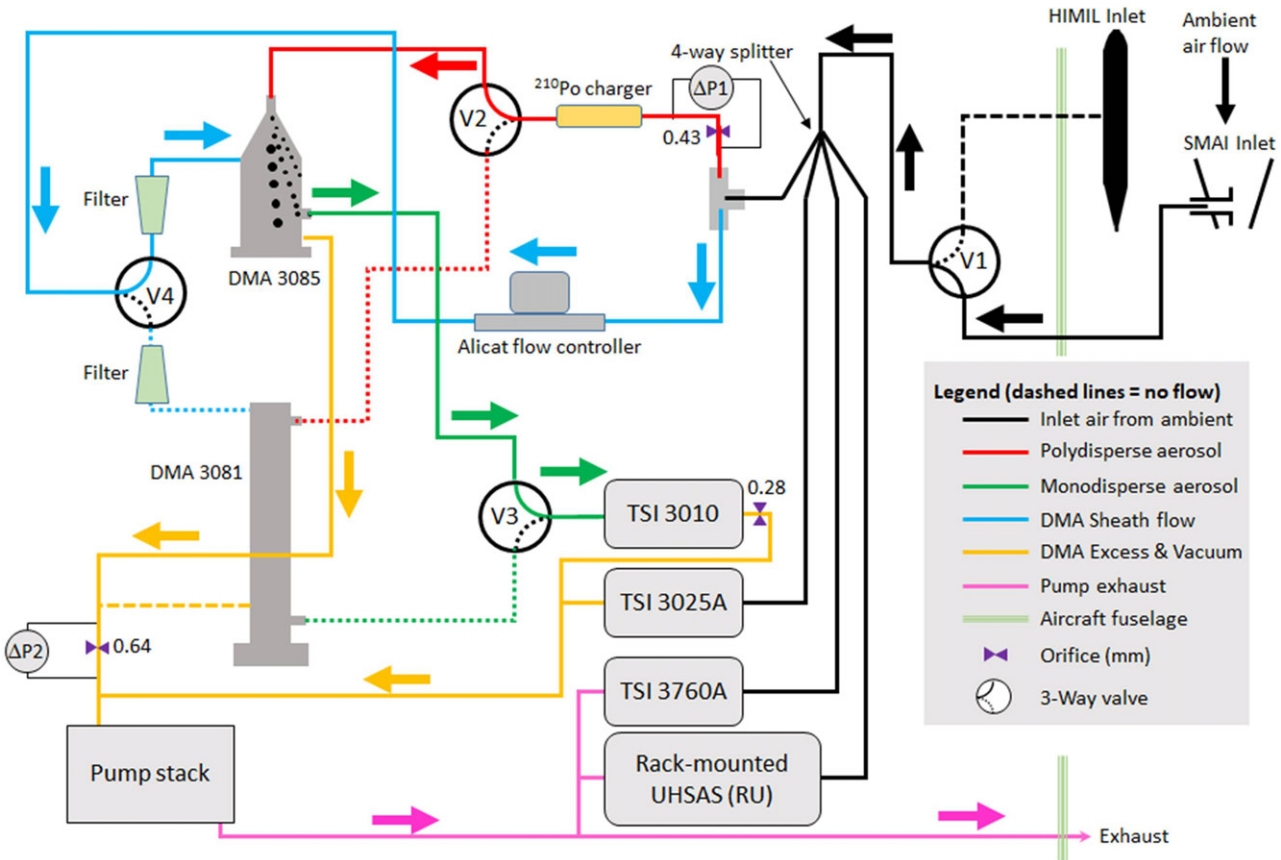


Figure 1. Instrument layout for aerosol sampling from the NSF NCAR C130 aircraft during ARISTO 2016. Manual valves were used to switch between inlet type (HIMIL or SMAI) and also DMA type (long-column or nano) for the SMPS. Thick arrows show the flow path of one of the configurations. In this example, inlet flow (black) from the SMAI inlet is used for all instruments. The polydispersed aerosol flow (red) and sheath flow (blue) are directed to the nano-DMA. The monodisperse particles (green) are then directed to the TSI 3010 CPC for counting. DMA excess flow and vacuum lines are shown in gold. The pump stack on the left-hand side of the figure controls the flow through the TSI 3025 A and the SMPS (including the 3010 CPC). The 3760A and UHSAS have their own dedicated pumps. Each rack-mounted instrument shared a common exhaust line as indicated by the pink lines.

of improved airborne observational capabilities. Each ARISTO campaign typically operates for 10–20 flight hours over a several week period. The program uses both the Gulfstream V (UCAR/NCAR – Earth Observing Laboratory 2005) and the C-130 (UCAR/NCAR – Earth Observing Laboratory 1994), depending on scientific objectives and the availability of these platforms.

There were several goals of the aerosol measurements during ARISTO 2016. The first goal was to compare the size distributions between the NCAR scanning mobility particle sizer (SMPS) and two different Ultra-High Sensitivity Aerosol Spectrometer (UHSAS) instruments. These instruments measure different particle diameter ranges, so we were particularly interested in the overlap region and how a combination of the two instruments can be used to obtain a nearly complete size distribution for particles ranging from less than 10 to 1,000 nm in diameter. The second

objective was to compare aerosol properties from the two different UHSAS instrument – one of which was rack-mounted (RU) and the other was wing-mounted (WU). Third, we wanted to compare total integrated particle concentrations derived using the SMPS and UHSAS with the particle number concentrations measured by two different condensation particle counters (CPCs). And fourth, two different aircraft inlets were used for all cabin instruments and were compared to determine if there were any biases in sampling and transmitting the aerosol particle stream.

2. Experimental

The five instruments described above were used to sample aerosol particles from a variety of different conditions encountered in flight (Figure 1). The SMPS, two CPCs and the RU shared a common inlet, whereas the WU contained its own integrated inlet.

Table 1. Summary of aerosol sampling instrumentation for the 2016 Airborne Research Instrumentation Testing Opportunity (ARISTO) campaign.

Instrument short name	Long name	Measurement type	Diameter range	Sampling frequency	Other
SMPS (NCAR ACOM and EOL RAF)	Scanning mobility particle sizer	Particle size distributions	8–110 nm or 21–370 nm ^a	30 s	Regular DMA or nano-DMA; 15 diameter channels
WU: (Wing-mounted UHSAS; NCAR EOL RAF)	Ultra-high sensitivity aerosol spectrometer	Particle size distributions	60–1,000 nm	1 s ^b	Integrated inlet
RU (Rack-mounted UHSAS; University of Wyoming)	Ultra-high sensitivity aerosol spectrometer	Particle size distributions	55–1,000 nm	3 s ^b	Shared inlet, 99 diameter channels for both RU and WU.
CN Counter (NCAR EOL RAF)	TSI condensation particle counter, model 3760A	Total particle number counts	$D > 11$ nm	1 s	50% particle collection efficiency at 11 nm diameter
TSI 3025A CPC (NCAR ACOM and EOL RAF)	TSI ultra-fine condensation particle counter, model 3025A	Total particle number counts	$D > 3$ nm	4 s	50% particle collection efficiency at 3 nm diameter

Note. Instrument operator and institution are shown in parentheses with abbreviations defined below the table.

^aThe two ranges listed indicate the diameters for two different configurations: nano-differential mobility analyzer and regular (long-column) differential mobility analyzer. See Figure 1 for plumbing diagram.

^bThe sampling frequency of UHSAS instruments is variable and controlled by the user. The values listed here are not an inherent property of the instrument, rather only what was chosen for this campaign.

Abbreviations: NCAR: National Center for Atmospheric Research; ACOM: NCAR Atmospheric Chemistry Observations and Modeling Laboratory; EOL: NCAR Earth Observing Laboratory; RAF: NCAR Research Aviation Facility.

For the four rack-mounted instruments, the choice of inlet as well as the SMPS sampling paths were controlled in flight by the operator using large diameter (3/8 in.) manual three-way valves (Swagelok SS-44SX6) that were mounted on the instrument panel. The SMPS was used to classify particles using either a long-column differential mobility analyzer (DMA; TSI, Inc., model 3081, Shoreview, MN, USA) or a nano-DMA (TSI, Inc., model 3085). Given the sheath flow rates and voltage limits for each DMA, the mobility diameters that could be sampled with these two configurations were ~8–110 and ~20–350 nm for the nano-column and long-column DMA, respectively. The diameter range is approximate because it is partially a function of DMA pressure, which changes with altitude during flight. This effect is discussed in Section 2.2. The two different UHSAS (Droplet Measurement Technologies) were used for measuring particle size distributions between 55 and 1,000 nm (see supplementary information [SI] Table 2S for specific diameter channels for each instrument). Two butanol-based CPCs, also known as condensation nucleus (CN) counters, were used to sample integrated particle number concentrations (cm^{-3}) from the ambient air. The first one was a model 3760A (TSI, Inc.) with a 50% counting efficiency cutoff diameter (D_{50}) of 11 nm. The second CPC was a model 3025A (TSI, Inc.), often referred to as an ultra-fine particle counter that has a D_{50} of 3 nm (Stolzenburg and McMurry 1991). The instrument configuration is shown in Figure 1. More details about the measurements and inlets are included below and are summarized in Table 1.

2.1. HIMIL and SMAI inlets

An inlet is required to bring in atmospheric gases or particles to instruments located inside the aircraft cabin. Transmission efficiency and discrimination are potential issues of all inlets (Porter et al. 1992; Sheridan and Norton 1998). A photograph of the two inlets used for this experiment is shown in Figure S1 (SI). The GV High-performance Instrumented Airborne Platform for Environmental Research (GV HIAPER) Modular Inlet (HIMIL; UCAR/NCAR – Earth Observing Laboratory 2007) is a flow through inlet that has a diffusing nozzle on the upstream side and a converging nozzle on the aft end. It is designed to provide isokinetic sampling of gases and aerosol particles. Fluid dynamics calculations show that at typical aircraft speeds for either the GV or C-130 aircraft (~110–200 m s^{-1}), particle losses within the HIMIL diffuser are less than 10% for particles between 100 and 1,000 nm between 0 and 12,000 m altitude. Predicted losses are less than 5% for particle sizes analyzed by the SMPS (~10 to 100 nm; Air Sample Inlets; UCAR/NCAR – Earth Observing Laboratory 2011), however, there can be other size-dependent diffusional losses between the inlet and the rack-mounted instruments in the cabin (Hermann et al. 2001) as well as inefficiencies based on particle composition (Sheridan and Norton 1998). With any type of inlet where the free stream flow velocity is reduced, there is a necessary amount of heating (“ram heating”) where sample temperatures rapidly increase as the free stream velocity is compressed (Wilson et al. 1992). This has the potential to reduce particle

mass due to the evaporation of aerosol-bound volatile species including water (Porter et al. 1992). These effects were not the focus on this study, but it is important for researchers to be aware of these possibilities. The submicron aerosol inlet (SMAI) was designed to sample particles while traveling through clouds and minimize interference from shatter artifacts from either liquid or ice particles. A detailed description is given in Craig et al. (2013) and only a few details are discussed here. The SMAI is shaped like a truncated cone with the wider diameter (ID = 6.35 cm) facing forward. A sub-sampling tube (1.27 cm diameter, 6.86 cm downstream of the entrance) penetrates into the center of the inlet, perpendicular to the main flow. The smaller aft end of the SMAI has an inner diameter of 2.22 cm where the main flow exits. During typical flight speeds of the C-130 ($100\text{--}150 \text{ m s}^{-1}$), the forward facing inlet creates a higher pressure zone which reduces the flow to $\sim 10 \text{ m s}^{-1}$ inside the entrance region. The air then accelerates to $\sim 40 \text{ m s}^{-1}$, from which the sample flow is drawn. Numerical calculations predict the cutoff size for particles entering through the SMAI to be $3 \mu\text{m}$ for these conditions. The SMAI and the HIMIL are both considered suitable for aerosol sampling from the C-130, while the GV aircraft specifically uses HIMIL inlets. Downstream of the inlets, the sample passed through a four-way flow splitter with a 3/8 in. OD inlet and four individual 1/4 in. outlet ports (Brechtel Manufacturing, model 1104). This splitter distributed the sample flow into the RU, the SMPS and the two CPCs according to each instrument's flow requirement (see Figure 1).

2.2. Scanning mobility particle sizer

The SMPS is a common instrument that measures particle size distributions based on electrical mobility (Wang and Flagan 1990; Flagan 2011). Some pertinent background information is provided here with additional details listed in the SI. The airborne NCAR SMPS measures a portion of the total particle size distributions over the approximate mobility diameter range of 8–350 nm. There are two primary components: a DMA that separates the particles into individual sizes from an original polydispersed distribution, and a CPC, which counts the separated particles and evaluates their size-resolved concentration. Before entering the DMA, the aerosol is drawn through a ^{210}Po charge conditioner, which places a well-defined (Fuchs) charge distribution on the particles. The DMA uses a combination of particle-free sheath air and time-

varying high voltage applied to its center rod to select single mobility particles, which then travel through the DMA's exit port to be counted by the CPC. This aircraft SMPS has a 30 s one-way scan time covering 15 logarithmic-based equally spaced diameter channels. The raw data is an array of time-dependent and mobility-classified particle counts over each counting interval. This data is mathematically inverted during post-flight processing to obtain the particle size distributions. This instrument was originally built between 2011 and 2012 and first flew on the 2012 DC3 Mission (Barth et al. 2015) on the GV aircraft. It has also flown on the C-130 during the 2013 NOMADSS campaign in the southeast U.S. (Ye et al. 2016), in Colorado during the 2014 FRAPPÉ (Front Range Air Pollution and Photochemistry Experiment) study (Pfister et al. 2017) and the 2018 WE-CAN (Western Wildfire Experiment for Cloud Chemistry, Aerosol Absorption, and Nitrogen) experiment. The pre-2016 configuration only used the nano-DMA portion of the instrument (Figure 1) for better coverage of the smallest particles, and less redundancy with the UHSAS. For the 2016 ARISTO study, both DMAs were used to study all possible configurations of the instrument. When sampling polluted urban atmospheres or smoke plumes, there is the potential of introducing counting errors due to multiple charges on large particles. The probability of a 100 nm particle obtaining more than a single positive charge is less than 4% and is less than 2% for a 70 nm particle (Wiedensohler 1988), so this effect is neglected when only using the nano-DMA. However, when using the long-column DMA, an impactor installed upstream up the DMA inlet would help remove large particles thereby reducing this uncertainty. The DMA selection was performed by using a pair of manual valves (labeled V3 and V4 in Figure 1) and an indicating flag in the data system. The flag is necessary to correctly define the mobility diameters based on geometry, sheath flow, aerosol flow, instrument pressure, and voltage limits for the appropriate DMA. See the SI for additional details about the SMPS (including calibration, flow characterization, diameter ranges, CPC operation, and the mathematical inversion process).

2.3. Ultra-high sensitivity aerosol spectrometer

The UHSAS from the NCAR Research Aviation Facility (RAF) is a customized instrument mounted externally in a wing pod, while the other (University of Wyoming) is a standard instrument packaged for lab/field use. These are referred to as "WU" for the wing-mounted UHSAS and "RU" for the rack-

mounted UHSAS, respectively. The RU drew air from the same inlet as the other cabin instruments (Figure 1). The WU was mounted on a pylon below the left wing tip 42 cm below the skin, and has its own dedicated inlet in the free air stream. The UHSAS measures scattering produced when aerosol particles are drawn through light emitted by a solid-state laser ($\lambda = 1,054$ nm). The scattered light is collected by two pairs of Mangin mirrors and a combination of calibration and Mie theory is used to classify particles into different size channels (Cai et al. 2008). The procedures used for calibrating the RU are described in detail in Fults et al. (2019) and only relevant details are listed here. Similar calibrations were performed with the wing-mounted unit. A separate SMPS was used to obtain monodisperse test aerosols at RH < 15%. The primary particle composition was ammonium sulfate. The refractive index of this material at $\lambda = 1.05 \mu\text{m}$ is $n = 1.51$ (Toon et al. 1976). In this testing, the mode diameter measured by the UHSAS (65 nm) is smaller than that reported by the SMPS ($D = 75$ nm). This difference is qualitatively consistent with the smaller refractive index of the test material (ammonium sulfate), compared to the larger refractive index of the polystyrene latex particles used by the manufacturer. During ARISTO 2016, there were 99 diameter channels spanning 60–1,000 nm for the WU and 55–1000 nm for the RU (SI Table S2).

2.4. Condensation particle counter

The standard RAF CPC is a butanol-based model 3760A particle counter (TSI, Inc.) with a 50% cutoff diameter of 11 nm. A diaphragm pump (Gast Manufacturing, Inc., model DOA-V191-AA) pulls the air sample from the inlet through the instrument before being exhausted outside the aircraft. Sample flow is controlled by a 1.5 L min^{-1} critical orifice at the back of the counter. For aircraft use, a Rosemount 1201F pressure transducer, an AD590 temperature sensor and a 0-2 SLPM mass flow meter (Sierra Instruments, Inc.) have been added to quantify the volumetric flow rate through the instrument (Twohy 1991) in order to calculate particle concentration.

2.5. Ultrafine condensation particle counter

The TSI 3025A ultrafine condensation particle counter has historically been a standard instrument for detecting particles as small as 3 nm in diameter (Stolzenburg and McMurry 1991) and has been used extensively for ambient monitoring especially when

identifying and characterizing nucleation and new particle formation events (Cheng 2011). This model differs from traditional butanol-based CPCs in that the inlet flow is split between a filtered (particle-free) sheath flow and a capillary flow that contains the ambient aerosol. The capillary flow is injected into the middle of the surrounding sheath flow, the latter of which is saturated with butanol vapor. Both air streams are combined and then transferred to the condenser region, where the particles grow to sizes that can be detected by the combination of a laser diode and photodetector inside a heated optics block. The capillary flow is confined to the center line of the flow path where there is a higher butanol supersaturation than near the walls. This results in the 3025's ability to detect particles as small as 3 nm. For ground-based applications, the instrument is calibrated so that the volumetric inlet flow is 300 ml min^{-1} with 270 ml min^{-1} split off as the sheath flow and the remaining 30 ml min^{-1} becoming the capillary flow. The total flow as well as the split ratio is controlled by a combination of pumping speed and valves that are adjusted during flow calibration. With constant pumping speeds and inlet conditions, these flows remain relatively stable. In aircraft applications, however, the total inlet flow (sheath + capillary) can change, and the ratio between the two can also change. In order to accurately measure particle concentrations, these flows need to be well-characterized. For the ARISTO 2016 measurements, the particle number concentrations were initially calculated assuming the sheath and condenser flows were the same as those done during preflight calibration. Altitude-dependent flow corrections were later applied to adjust these concentrations to actual flow conditions, and the results are discussed below in Section 4.1. The procedure for characterizing the TSI 3025 flows is described in Section S2 in the SI.

3. Mission specifics

The ARISTO 2016 mission consisted of six individual research flights (RF01–RF06) during August 2016 on the NSF C-130 (UCAR/NCAR – Earth Observing Laboratory 1994). All flights started and ended at the Rocky Mountain Metropolitan Airport. This is the home of the NCAR Research Aviation Facility (RAF) in Broomfield, Colorado (39.91°N , 105.12°W , 1719 MSL). The total payload consisted of a number of gas-phase and particle-phase instruments, stabilized platforms, state parameters, radiation measurements, LIDAR, and dropsondes for atmospheric vertical

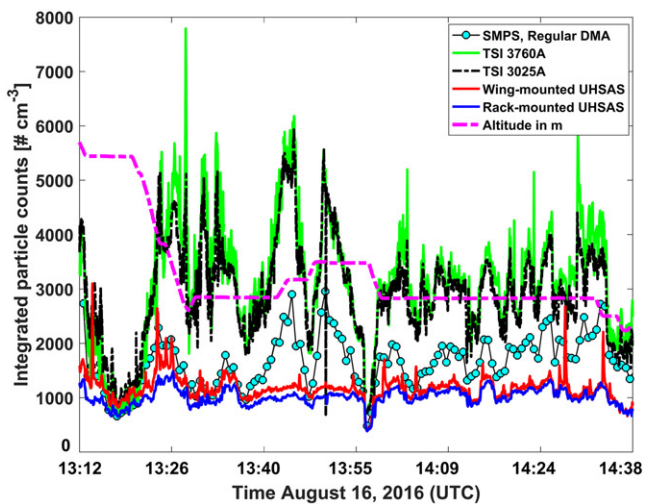


Figure 2. RF06 time series of integrated particle concentrations from five different instruments: SMPS using the regular (long-column) DMA (see Figure 1), two different CPCs (TSI 3025A and 3760A), and the two different UHSAS as indicated in the plot legend. All cabin instruments used the SMAI inlet for this example.

profiling. In order to accommodate the various research objectives, flight hours were divided up into cloud sampling, urban/boundary layer conditions, aircraft maneuvers, forest fire plumes, remote continental air and marine boundary layer air. Flights RF01–RF05 were fairly short (1–3 h each), whereas RF06 went all the way to the west coast and was 11.6 h in duration. There was a total of 21.4 flight hours. The individual flight maps are shown in the SI (Figures S15–S20). A brief summary of the flights is listed in the SI (Table S1).

4. Results

4.1. Condensation particle counter comparisons

All particle measurements reported in the following sections are at conditions of the SMPS where there were continuous temperature and pressure measurements that were applicable for the cabin instruments sharing the same inlet as shown in Figure 1. The one exception is the wing-mounted UHSAS, which is discussed in Section 4.2. Figure 2 shows a time series of particle concentrations from RF06. The SMPS data are at 30 s time intervals and the other instruments' data have been averaged over 10 s. The two CPCs generally agree and are higher than the SMPS integrated concentration. The RU and WU instruments also show good agreement and show the lowest particle concentrations among the instruments over this time period. This indicates that at least half of the CPC-measured particles are smaller than can be detected by the UHSAS, and that the regular SMPS does not capture the entire size range of the ambient aerosol

distribution. In this case, the SMPS used the long-column DMA with a size range of ~21–370 nm.

There is generally good agreement between the TSI 3025A and the 3760A, but there are some discrepancies. Figure 3 shows a series of scatter plots during RF06 with the TSI 3760A particle concentrations on the *x*-axis and the TSI 3025A concentrations on the *y*-axis. The first panel (a) is all data for the 11.6 h flight as it was collected. The next panel (b) is the same data except that the TSI 3025A data has been corrected using the derived condenser and capillary flows as discussed in SI Section S2. Finally, panel c shows a portion of this data taken from 14 cloud-free constant-altitude legs. We make this latter comparison because transient flows within the instruments (primarily the 3025) during altitude changes cause greater uncertainties in the concentration calculations before the flows reach steady state. The agreement between the two instruments is improved with a slope of 1.01 and an R^2 value increasing to 0.97 with the constant-altitude constraint. However, there are a few outliers, and it is instructive to investigate their origin.

These same constant-altitude legs were analyzed by taking the ratio of the TSI 3760A concentrations to the TSI 3025A concentrations and plotting the ratio vs. altitude (Figure 4a). The average ratio is slightly greater than 1.0 at lower altitudes and is within a few % of 1.0 at altitudes of 2,800 m and higher. Figure 4b shows the same data as a scatter plot of this ratio versus particle concentration, and colored by altitude. At least two details are evident from this analysis. First, the concentrations observed at the lowest two altitudes

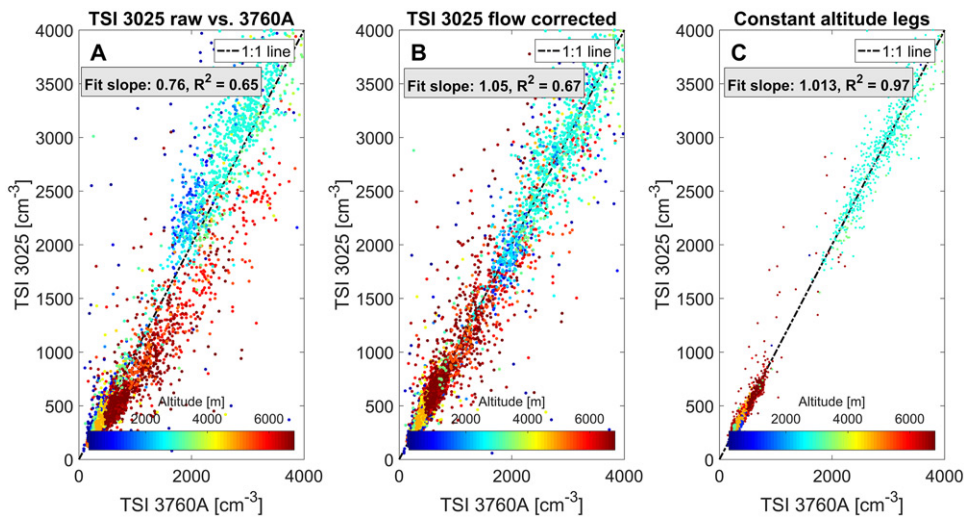


Figure 3. Scatter plots of total particle concentrations from the TSI 3025A and the TSI 3760A CPCs during RF06. (a) All data as collected. (b) The same data after the 3025 A concentrations were adjusted by correcting the flows as indicated in SI Figure S4. (c) The correlation for 14 separate constant-altitude legs and removing data points that were sampled during periods where the plane was in clouds. These latter two constraints reduced the original 8890 data point pairs to 3475.

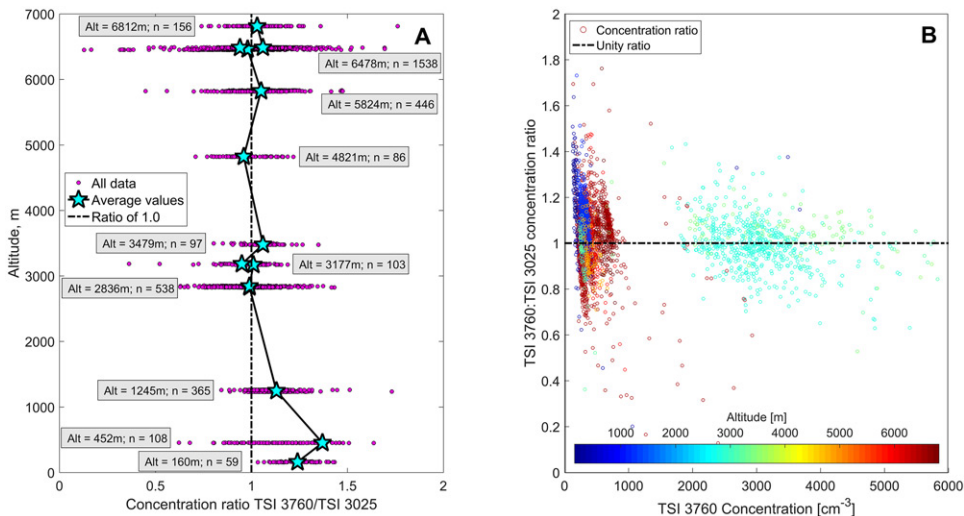


Figure 4. Comparison of particle concentrations measured by the TSI 3025 and 3760 CPCs. (a) The ratio of particle number concentration for TSI 3760 to TSI 3025 for 10 constant-altitude legs during ARISTO Research Flight 6. The altitude (in m) and number of data point pairs (n) are indicated in the gray boxes. The two CPCs shared a common inlet, and both data sets were calculated as number per cm^3 using the volume calculated from the temperature and pressure within the SMPS. (b) The same ratio plotted against TSI 3760 particle concentration, which demonstrates that there is generally more variability at lower particle concentrations, at high altitude (5,000–6,500 m) and at low altitudes including the marine boundary layer.

were over the Pacific Ocean off the Oregon coast (see SI Figure S20) or at high altitude (>6,000 m) where the concentrations were generally low (less than $1,000 \text{ cm}^{-3}$), which limits counting statistics. Second, the average ratio is consistently greater than 1.0 at the lowest three altitudes, which we believe is due to uncertainties in flow rates at these altitudes. Recall from SI Section S2 and Figure S4, the 3025 sheath, condenser and capillary flows were derived using empirical relationships based on laboratory

measurements from ambient pressure ($\sim 830 \text{ hPa}$ in Boulder, CO) to 350 hPa , and that flows at pressures below that altitude were extrapolated. Since the actual flows at $\sim 1,000 \text{ hPa}$ are unknown, and it was not possible to test these situations in the NCAR laboratories, we are pointing out this limitation. We choose to not artificially (and possibly incorrectly) correct the data using flow rates for the lower altitude legs that were not experimentally verified. Other than these periods and approximately 50 outlying data point pairs (out

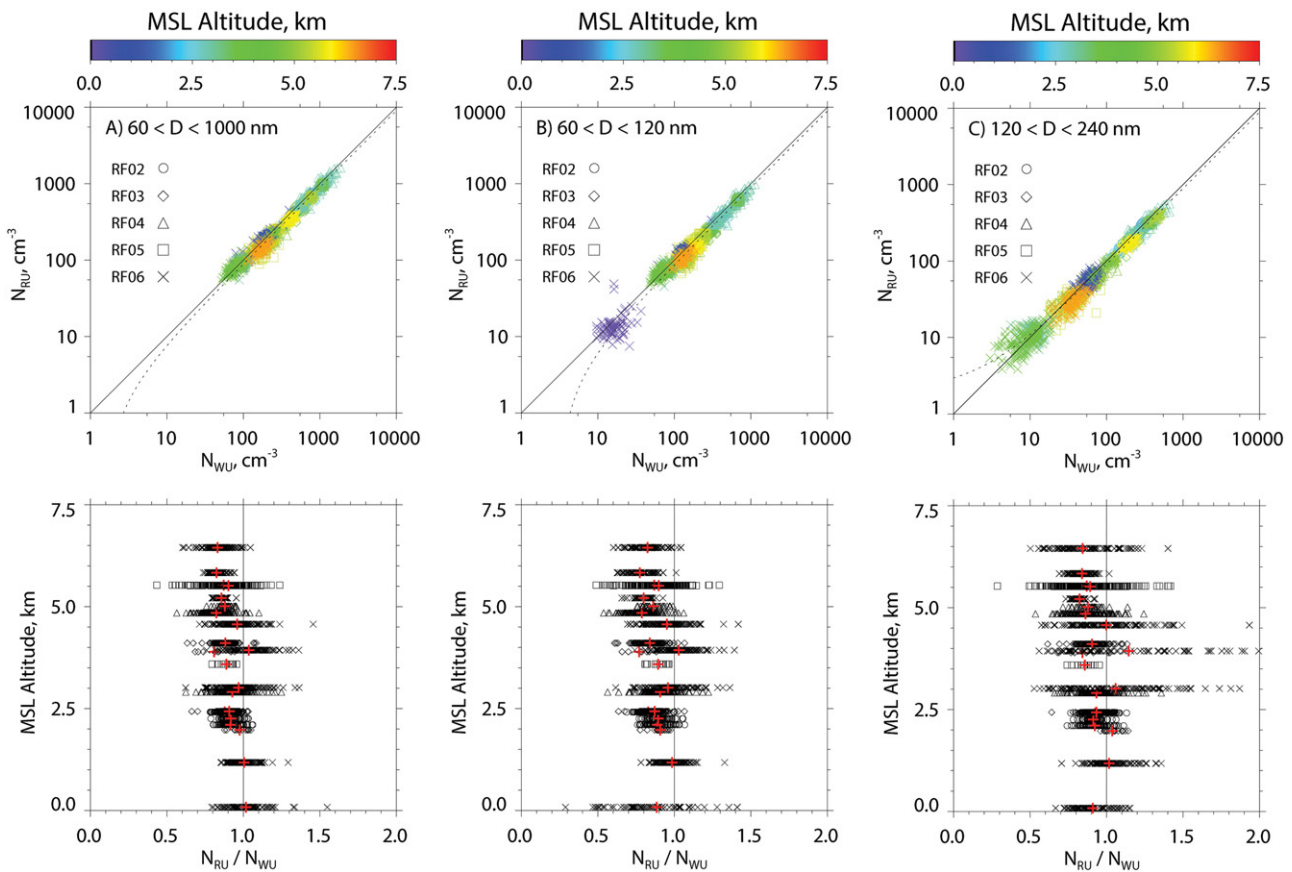


Figure 5. RU and WU particle concentrations for constant-altitude and cloud-free segments of RF02–RF06. The upper panels compare the RU integrated particle concentrations to those of the WU for the diameter ranges listed. The solid line is 1:1 (perfect agreement) and the dashed line is the least-squares fit. The lower panels show the concentration ratio (N_{RU}/N_{WU}) as a function of altitude for the same diameter ranges. The red crosses indicate the average values at each altitude level. Table S3 in the SI section provides the UTC time intervals, altitude, and number of data points per flight segment.

of 3,475), the agreement between the two CPCs' concentrations is within 12%.

4.2. UHSAS comparisons

Aerosol sample flows were controlled differently between the WU and RU. Because of this difference, as well as the different locations on the C-130 (Figure 1), our comparison of WU and RU particle concentrations involves pressure-dependent and temperature-dependent adjustment factors. The WU aerosol stream was controlled to a preset volumetric flow rate (\dot{V}_{WU}) of $50 \text{ cm}^3 \text{ min}^{-1}$ at the conditions of the optical block temperature (T_{WU}) and Pressure (P_{WU}). The WU aerosol flow rates were adjusted to the conditions of the aircraft rack-mounted instruments using Equation (1):

$$(\dot{V}_{WU})' = \dot{V}_{WU} \cdot (T_{AL}/T_{WU}) \cdot (P_{WU}/P_{AL}) \quad (1)$$

Here $(\dot{V}_{WU})'$ is the adjusted volumetric aerosol flow rate and T_{AL} and P_{AL} are the temperature and pressure values reported by the SMPS Alicat flow

controller (Figure 1). We calculated WU particle concentrations as the WU particle counts divided by $(\dot{V}_{WU})'$. Over all level-flight segments, the adjustment factor (i.e., $(T_{AL}/T_{WU}) \cdot (P_{WU}/P_{AL})$) varied between 0.88 and 1.02.

The RU aerosol stream was controlled to a preset volumetric flow rate of $52 \text{ cm}^3 \text{ min}^{-1}$, which can vary slightly due to changes in ambient conditions. This instrument records the mass flow rate. The actual volumetric flow rate was derived based on this mass flow rate along with pressure and temperature. The RU particle concentrations were then calculated the same way as listed above for the WU.

Figures 5a–c show the RU and WU size-integrated particle concentrations for diameters between 60–1,000 nm, 60–120 nm, and 120–240 nm, respectively. These were taken from level-flight and cloud-free segments of RF02–RF06. The time intervals, altitude and number of data points per flight segment are provided in the SI (Table S3). The upper panels compare concentrations from the two instruments. Here, the solid lines indicate 1:1 agreement and the dotted

Table 2. Diameter limits for overlap region between the largest three size channels of the SMPS and the smallest three adjusted size channels of the Rack-mounted UHSAS (RU).

Channel Designator	SMPS Lower-limit diameter nm	SMPS Upper-limit diameter nm	SMPS Midpoint diameter nm	RU Lower-limit diameter nm	RU Upper-limit diameter nm	RU Midpoint diameter nm
A	56	67	62	56	67	61
B	67	82	75	69	82	75
C	82	98	90	84	100	92

Note. The SMPS mobility diameters change with ambient conditions (SI Figure S3). These table entries are calculated using 85 kPa for the DMA pressure, 22 °C for temperature and 3.3 L min⁻¹ for both the sheath and excess DMA flows.

lines are the linear least-squares fit of the data. The slopes of the fit lines range from 0.89 (± 0.01) (Figure 5c) to 0.90 (± 0.01) (Figure 5a), and the intercepts range from -3 (± 2) (Figure 5b) to 2 (± 1) (Figure 5c). In the lower panels, concentration ratios (N_{RU}/N_{WU}) are plotted versus altitude with the red symbols indicating the mean values. This ratio generally decreases with increasing altitude. The lowest-altitude and highest-altitude ratios are exclusively from RF06, but it is apparent that ratios from the other flights show the same pattern. An exception to the negative altitude trend is apparent at the lowest altitude where the average ratio shifts to ~ 0.9 at 80 m MSL in a marine boundary layer (see flight map of RF06 in Figure S20 in the SI). Our understanding of the ratio's altitude dependence is limited. Possibilities include biases associated with the WU and RU flow rate measurements and their temperature-dependent and pressure-dependent adjustments, differences in transmission efficiency in the separate inlets, refractive index changes associated with particle drying during transmission to the scattering volume (Sheridan and Norton 1998), and differences in detection efficiency, particularly at diameters smaller than ~ 80 nm (Kupc et al. 2018). Altitude trends in N_{RU}/N_{WU} are consistent in total concentration and in the size-resolved data, suggesting that the differences are independent of the size ranges analyzed. Concentrations of particle diameters larger than 240 nm were generally too low to make statistically meaningful comparisons.

4.3. SMPS-UHSAS comparisons

Particle size distributions represent particle concentrations classified into discrete size channels within a period of time. Following the aerosol science convention for representing size distributions (Hinds 1982), we present the difference form of the distribution ($\Delta N/\Delta \log_{10}D$) on the y -axis and diameter (D) on the x -axis. If a distribution is numerically integrated over all detected diameters, the result is a size-integrated concentration (N , cm⁻³). In order to compare UHSAS- and SMPS-derived values of $\Delta N/\Delta \log_{10}D$ it is

necessary to select channel diameter boundaries that are the same, or nearly the same, for the compared instruments. Since the denominator of the difference form of the distribution is expressed in terms of logarithm of D , we strived to make equally spaced diameter channels ($\Delta \log_{10}D = \log_{10}(D_{i+1}/D_i)$) where i is the bin number, from both instruments. The SMPS distributions span particle diameters from ~ 8 to 91 nm, over 15 channels (Table 1). To match this, we combined bins from the UHSAS distributions (both UW and RU) to best match the SMPS values of $\log_{10}(D_{i+1}/D_i)$. In other words, the original UHSAS diameter spacings of $\log_{10}(D_{i+1}/D_i) = 0.012$ (WU) and $\log_{10}(D_{i+1}/D_i) = 0.013$ (RU) were adjusted to approximately match the SMPS value $\log_{10}(D_{i+1}/D_i) = 0.086$ while preserving the total number of particles observed. This re-classification resulted in three channels from the smallest diameters of the UHSAS distributions that approximately overlapped with three channels from the largest diameters from the SMPS distributions. The midpoints of the overlapping channels do not match exactly, but they are in reasonable agreement.

- Overlap midpoint diameter Channel A: $D(\text{SMPS}) = 62$ nm, $D(\text{RU}) = 61$ nm
- Overlap midpoint diameter Channel B: $D(\text{SMPS}) = 75$ nm, $D(\text{RU}) = 75$ nm
- Overlap midpoint diameter Channel C: $D(\text{SMPS}) = 90$ nm, $D(\text{RU}) = 92$ nm

The midpoint, upper and lower diameter limits for these channels from the two instruments are summarized in Table 2. The complete list of the original and adjusted diameter channels from the two UHSAS instruments is given in the SI (Table S2). It should be pointed out that the particle sizes reported by the SMPS are electrical mobility diameters, which can differ from aerodynamic diameters (DeCarlo et al. 2004) and optical equivalent diameters (Cai et al. 2013) depending on particle composition, density, shape, and morphology. In addition, the particle mobility through a DMA is a function of pressure, which was

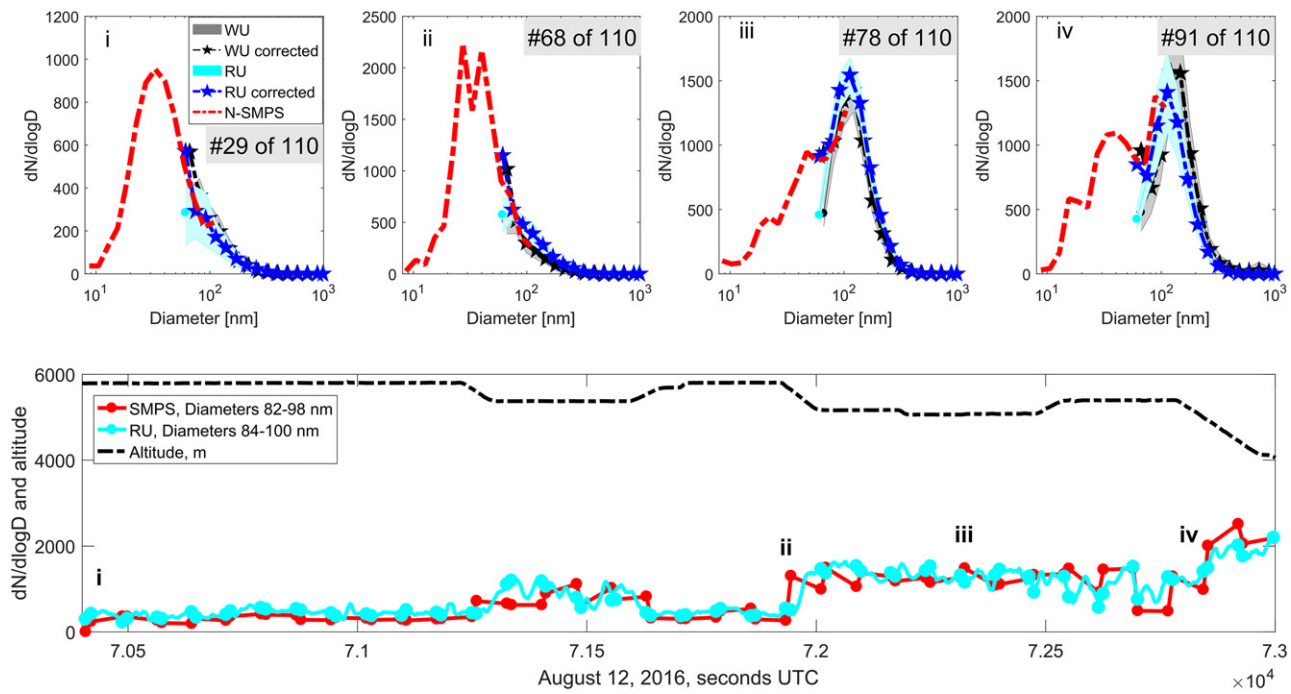


Figure 6. Time series of $\Delta N/\Delta \log_{10}D$ values from SMPS and UHSAS for the C channel (Table 2) taken during RF05 (12 August 2016). The upper four individual panels (i–iv) show representative SMPS, RU and WU size distributions ($\Delta N/\Delta \log_{10}D$ vs. D) for four periods during a 42 min portion of RF05 over north-central Colorado (SI Figure S19). In the lower figure, red markers are the SMPS data, while the cyan data is from the RU. Altitude is indicated by the dashed black line. In the size distribution panels, the gray and light blue areas show the mean and standard deviation of the UHSAS measurements over the 30 s time period for which the SMPS scan took place, and the solid black and blue symbols represent the corrected UHSAS average values for the WU and RU instruments, respectively. The UHSAS counting efficiency corrections are discussed in Sections 4.3 and 5 and in SI Figure S21, which is why there are slight deviations from the shaded regions between ~ 60 and 90 nm. The UHSAS time series data in the lower panel were not corrected. The SMPS values are shown in red and the text in the gray boxes indicates the scan number of the total number of scans taken during this flight ($n = 110$). Odd numbered scans are up scans (voltage and diameters increasing) and even numbers represent down scans.

mentioned in Section 2.2 and demonstrated in the SI (Figure S3). The SMPS diameters listed above and in Table 2 are relevant for an altitude of 75 kPa ($\sim 2,500$ m) and 24°C . Another issue when comparing the size distributions is sampling frequency. The SMPS data are series of single-diameter composite distributions acquired over 30 s where each data point represents a 2 s sampling period. The WU and RU data cover the entire distribution at either 1 Hz (WU) or 0.33 Hz (RU) (Table 1). At a typical research flight speed of 110 m s^{-1} , the distance covered by the C-130 in 30 s is 3.3 km, so the focus of these distribution comparisons is background continental air masses sampled at nearly constant altitudes where particle populations and size distributions are less likely to have dramatic horizontal variability as they would in an urban area or in a smoke plume.

Figure 6 shows a time series of $\Delta N/\Delta \log_{10}D$ for the C channel (Table 2) taken from RF05 on 12 August 2016. Also included are four representative size distributions (i–iv) from this flight leg. The UHSAS values are derived by merging data obtained ± 15 s about the

midpoints of the 30 s SMPS scans. The shaded regions in the upper plots represent the mean and standard deviation of the UHSAS $\Delta N/\Delta \log_{10}D$ values, and the dark lines with pentagrams represent the corrected mean UHSAS values using the counting efficiencies described in Kupc et al. (2018). For particles greater than 80 nm, the correction is negligible, but has the effect of increasing particle counts between 55 and 80 nm, which is most evident in panels iii and iv. Figure S21 in the SI shows a close-up of panel iii to specify each curve, and better distinguish between the individual data points. SI Figure S22 shows the counting efficiency curve used to calculate the points. As can be seen by these four panels, this correction sometimes improves the overlap region between the SMPS and UHSAS. The actual size-dependent counting corrections are dependent on the particular instrument and particle composition, which for this mission are not known. So, we include some adjusted data to demonstrate that the two UHSAS instruments used here may require counting corrections for the lowest diameters, and that could improve agreement with the

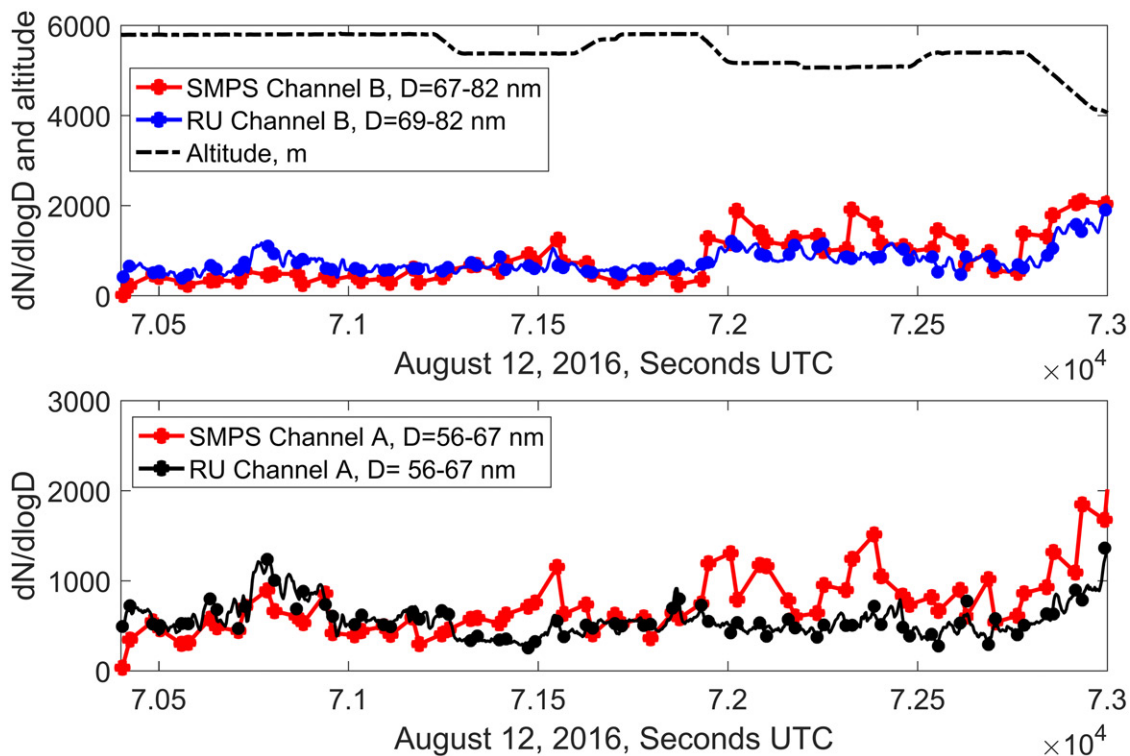


Figure 7. Time series of $\Delta N/\Delta \log_{10}D$ values from SMPS and RU for channels A and B during RF05 as discussed in Section 4.3. These correspond to SMPS particle diameters of 67–82 nm (top) and 56–67 nm (bottom) taken during RF05 on 12 August 2016. Similar to the values from channel C, the UHSAS data have not been corrected for counting efficiency.

SMPS in the overlap region. Other than the size distribution comparisons shown in panels i–iv in Figure 6, the UHSAS data presented here have not been corrected for counting efficiency.

Figure 7 shows the SMPS-UHSAS comparison for the A and B channels (Table 2) from the same flight – similar to the C channel described above. For the plots shown in these two figures, it should be pointed out that the SMPS values are closely spaced pairs instead of points at regular time intervals. This is because the C channel values of $\Delta N/\Delta \log_{10}D$ are evaluated three seconds apart as the DMA voltage is switched from the up scan to the down scan (i.e., increasing DMA voltage immediately followed by decreasing DMA voltage). This time interval is larger for the B channels (7 s), and larger yet for the A channel (11 s). Figure 8 shows the ratio of the $\Delta N/\Delta \log_{10}D$ values from the two instruments from the same time period. As can be seen, the ratio is generally close to 1.0, increasing to greater than 1.0 at a lower altitude for this example. An example of blending the two size distributions is shown in the color plot in Figure 9, which is the entire flight discussed in Figures 6–8. The lower portion of the plot shows the smallest particles from the SMPS, and the upper portion of the plot shows the UHSAS data. The three bins discussed

above from the UHSAS and SMPS are averaged, which is the section in the middle labeled as the overlap region. Additional data comparing the overlap region between the UHSAS and nano-SMPS for RF02–RF04 are shown in Figures S5–S7 in the SI.

4.4. Inlet comparisons

The final objective for this campaign was to observe the effect of switching inlets. A thorough inlet characterization involving size-dependent particle transmission efficiency is not possible with the ARISTO 2016 dataset, and we specifically limited our comparisons to cloud-free conditions. The goal here is to compare submicron integrated particle number concentrations using two common inlets sampling relatively uniform summertime air masses while at constant altitude. The SMAI and HIMIL were mounted adjacent to each other on the belly of the plane (SI Figure S1) and were switched by the operator from a manual three-way valve on the SMPS front panel (Figure 1). The inlet was switched between the HIMIL and SMAI for RF02–RF05, and was kept on the SMAI for the duration of RF01 and RF06. During these switches, there were times where a transient effect was noticed for a few seconds as the flows adjusted. Other than these

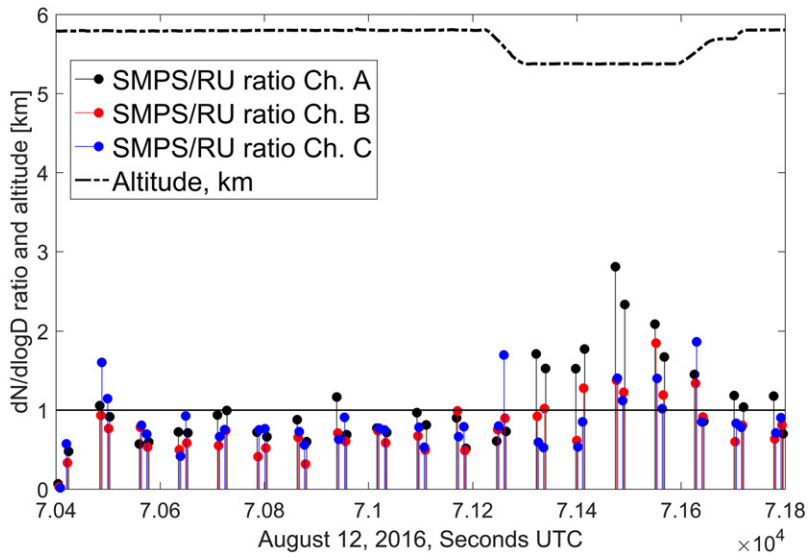


Figure 8. Ratio (SMPS/UHSAS) of individual $\Delta N/\Delta \log_{10} D$ values from Figures 6 and 7 (RF05) where the UHSAS chosen was the rack-mounted version (RU). UHSAS counting efficiency corrections were not applied when calculating these ratios.

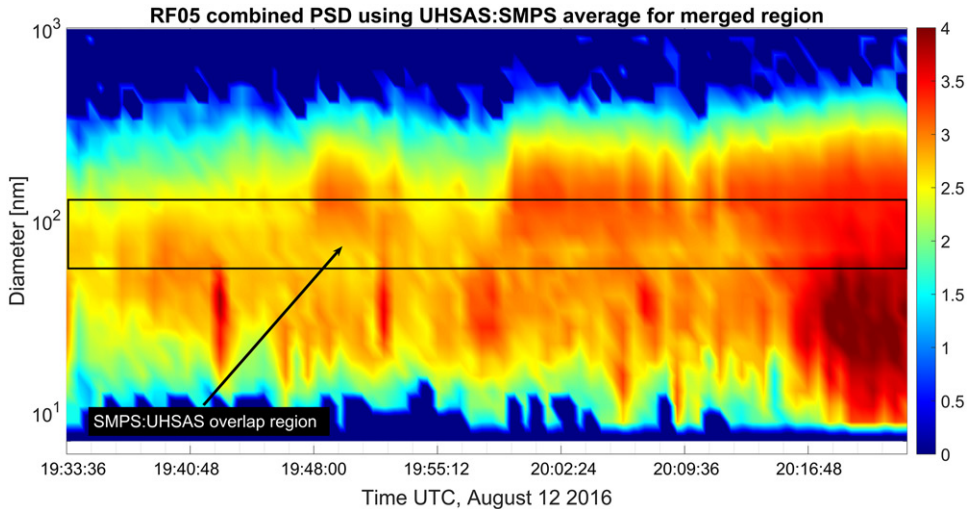


Figure 9. Color plot of blended SMPS and UHSAS particle size distributions (PSD) for RF05 on 12 August 2016. Time is listed on the x-axis, particle diameter is listed on the y-axis, and the color bar represents the logarithm of $\Delta N/\Delta \log D$ values (e.g., the orange color of 3 represents of $\Delta N/\Delta \log D = 10^3$). The UHSAS values are those using the diameter transformations discussed in Section 4.3, but were not corrected for counting efficiency.

occasions, there were no appreciable changes in particle concentrations between the two inlets, but on a moving platform with a changing aerosol population, it is not possible to completely separate out inlet effects from changes in particle size distributions. Figure 10 shows a representative case from RF03 where the inlet was switched from SMAI to the HIMIL during some vertical pitch maneuvers over northeast Colorado at $\sim 2,000$ MSL. It should be noted that ground level is $\sim 1,600$ MSL in this area, so these measurements were taken in the boundary layer. Each of the instruments (SMPS, UHSAS, and CPCs) showed no discernable change due to the switch.

Additional results from inlet switching are shown in the SI Table S4 and Figures S8–S14, and are discussed below.

5. Discussion

This manuscript contains the first detailed description of the NCAR aircraft SMPS instrument in the open literature. As it has acquired data during several recent aircraft campaigns, we believe it is important to document its design, capabilities, and representative data. We particularly wanted to extend the data analysis to show the overlap region between it and the

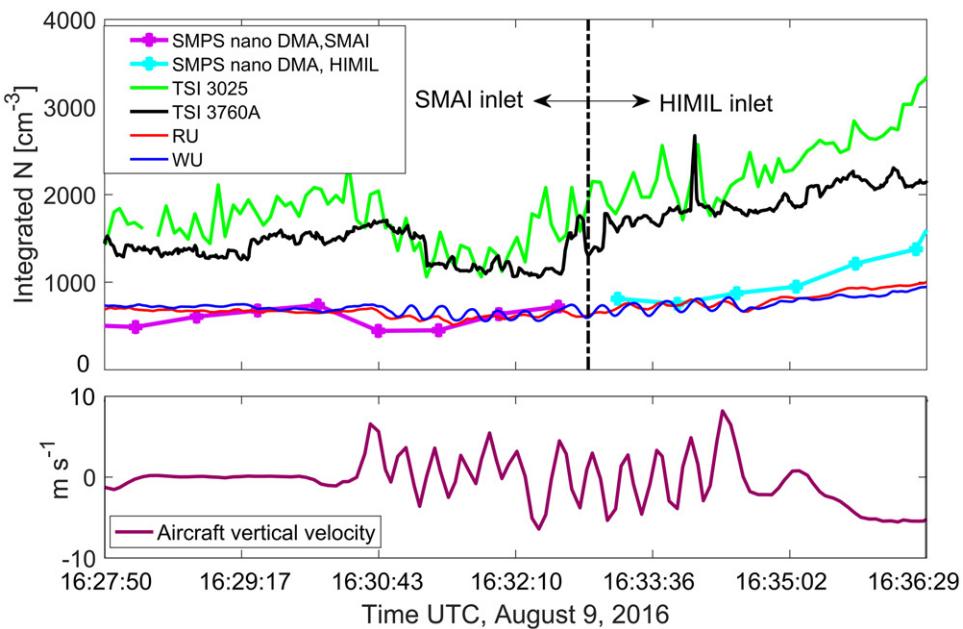


Figure 10. Comparison between HIMIL and SMAI inlets during vertical pitch maneuvers on RF03 (9 August 2016). The switch between inlets was made at 16:33 UTC. SMPS and UHSAS integrated particle counts are shown alongside total number counts recorded by the two CPCs (TSI 3760A and TSI 3025A). The data from the two CPCs and UHSAS have been averaged over 20 s to make the individual traces more clear. The altitude for these maneuvers was $\sim 2,000$ m. The lower plot shows the vertical velocity of the aircraft, with positive values indicating aircraft ascending motion.

UHSAS and show example data beyond the fundamental size distributions ($\Delta N/\Delta \log_{10} D$ vs. D), which have been submitted from previous NSF-funded and NASA-funded field campaigns. For background continental air, the analysis here demonstrates that there is adequate agreement in sizing information and particle number concentration when compared to the other instruments. The particle concentrations for the overlap region between it and the UHSAS generally agree to within 20%. The time series of UHSAS values shown in Figures 6–8 do not include the corrections discussed in Kupc et al., but were calculated using the original data and the adjustments discussed in Section 4.2. The relatively long (30 s) SMPS scan time in the current study is a limitation if sampling urban plumes, fires or other conditions where there is high spatial variability, but the response time of the modern mixing CPCs should allow scan times of < 10 s (Shah and Cocker 2005).

The model 3025A CPC showed excellent agreement with the model 3760A after correcting the capillary and condenser flows. There are different ways to account for capillary flow changes with altitude including adding flow meters in-line and logging the data as was done by Takegawa et al. (2017), or characterizing the flows as a function of measurement pressure and the differential pressure measurements within the instrument as was done for the current study. More modern CPCs such as the TSI model

3756 correct for this effect during sample collection. We focus the comparisons on horizontal cloud-free flight legs to minimize the added uncertainty arising from transient flows prior to reaching steady state due to altitude changes as well as non-uniform sample flows within the inlet that can result from different angles of attack (Murphy and Schein 1998). The differences between particle number concentrations were 12% or less for altitudes between $\sim 2,000$ m and 6,800 m (see Figure 4) with slightly greater variability at lower altitudes. Both CPCs were operated in such a way as to record pressure and temperature to accurately monitor sampling conditions, but there is inherent variability in those measurements with no evidence to conclude that one instrument is superior to the other. Rather, the conclusion here is that there is good agreement between the two instruments, which should be encouraging for future researchers wishing to incorporate CPCs into a sampling package. It should be noted, however, that although the model 3025A is capable of detecting smaller particles than the 3760A (Sections 2.4–2.5), it comes at the expense of poorer counting statistics due to the smaller 30 ml min^{-1} capillary flow versus the 1.5 L min^{-1} flow in the model 3760A.

Similar to the agreement in the CPCs, the measurements from the RU and WU also matched well. Integrated particle counts generally agreed within 20% for altitudes between 80 and 6,450 m (Figures 2 and

5) for particles in the size ranges discussed in [Section 4.2](#) (60–1000, 60–120, and 120–240 nm). The fact that they are completely separated and do not share the same inlet is especially encouraging. For these measurements, the calculations for particle number concentration at each size channel required the flows to be adjusted to a common thermodynamic state based on temperature and pressure measurements made immediately adjacent to the laser cavity as described in [Section 4.2](#). There is reduced counting efficiency for the smallest diameter channels within the UHSAS (Kupc et al. 2018), which are diameter-dependent, instrument-dependent, and composition-dependent. For the two UHSAS instruments discussed here, these efficiency values are not known, and because of instrument scheduling, it unfortunately is not possible to do a thorough side-by-side calibration. For comparing the overlap region between the UHSAS and SMPS size distributions shown in [Figure 9](#), the average of the two counting efficiency curves listed in Kupc et al. (2018) was used. But apart from the temperature and pressure adjustments indicated in [Section 4.2](#), the WU and RU comparisons were done with the “as-collected” data without further corrections.

Finally, we wanted to compare the HIMIL and SMAI inlets for aerosol sampling, as both are available for researchers using the NSF C-130. It is an important decision for researchers to make, and one that cannot easily be changed during a mission. ARISTO 2016 provided a rare opportunity to test the two side by side under a variety of different environments. [Figure 10](#) is one example that demonstrates that for the particle sizes and instruments used, there was no detectable change in number concentration or transmission efficiency. In this case, the average concentrations from each instrument before and after the switch agreed within 10%. This observation was repeatable on different research flights. Other examples of these switches from RF03-RF05 are listed in [Table S4](#) and [Figures S8–S14](#) in the SI. In addition, we used the non-parametric Wilcoxon Rank-Sum Test to evaluate the medians of the particle UHSAS particle concentrations before and after these inlet switches. In each case, the medians were statistically indistinguishable, indicating that particle transmission efficiency for $D > 400$ nm through both inlets is equal ($p > .05$, SI [Figure S14](#)). Based on these observations, we conclude that either inlet is suitable for submicron aerosol measurements ($D < 1,000$ nm) although the SMAI inlet likely provides improved sampling within clouds because this inlet reduces the bias caused by

unintentional detection of shattered liquid or ice hydrometeors.

Acknowledgments

The authors would like to thank the National Center for Atmospheric Research ARISTO program and the Research Aviation Facility staff for providing the opportunity, aircraft, and other infrastructure to perform these measurements. The National Center for Atmospheric Research is sponsored by the National Science Foundation. Any opinions, findings, conclusions or recommendations expressed in the publication are those of the authors and do not necessarily reflect the views of the National Science Foundation.

References

- Barth, M. C., C. A. Cantrell, W. H. Brune, S. A. Rutledge, J. H. Crawford, H. Huntrieser, L. D. Carey, D. MacGorman, M. Weisman, K. E. Pickering, E. Bruning, B. Anderson, E. Apel, M. Biggerstaff, T. Campos, P. Campuzano-Jost, R. Cohen, J. Crounse, D. A. Day, G. Diskin, F. Flocke, A. Fried, C. Garland, B. Heikes, S. Honomichl, R. Hornbrook, L. G. Huey, J. L. Jimenez, T. Lang, M. Lichtenstern, T. Mikoviny, B. Nault, D. O’Sullivan, L. L. Pan, J. Peischl, I. Pollack, D. Richter, D. Riemer, T. Ryerson, H. Schlager, J. St. Clair, J. Walega, P. Weibring, A. Weinheimer, P. Wennberg, A. Wisthaler, P. J. Wooldridge, and C. Ziegler. 2015. The deep convective clouds and chemistry (DC3) field campaign. *Bull. Am. Meteorol. Soc.* 96 (8):1281–1309. doi:[10.1175/BAMS-D-13-00290.1](https://doi.org/10.1175/BAMS-D-13-00290.1).
- Cai, Y., D. C. Montague, W. Mooiweer-Bryan, and T. Deshler. 2008. Performance characteristics of the ultra high sensitivity aerosol spectrometer for particles between 55 and 800 nm: Laboratory and field studies. *J. Aerosol Sci.* 39 (9):759–769. doi:[10.1016/j.jaerosci.2008.04.007](https://doi.org/10.1016/j.jaerosci.2008.04.007).
- Cai, Y., J. R. Snider, and P. Wechsler. 2013. Calibration of the passive cavity aerosol spectrometer probe for airborne determination of the size distribution. *Atmos. Meas. Tech.* 6 (9):2349–2358. doi:[10.5194/amt-6-2349-2013](https://doi.org/10.5194/amt-6-2349-2013).
- Cheng, Y.-S. 2011. Condensation Particle Counters. In *Aerosol measurement: Principles, techniques, and applications*, eds. P. Kulkarni, P. A. Baron, and K. Willeke, 381–392. New York: John Wiley & Sons.
- Craig, L., A. Schanot, A. Moharreri, D. C. Rogers, and S. Dhaniyal. 2013. Design and sampling characteristics of a new airborne aerosol inlet for aerosol measurements in clouds. *J. Atmos. Ocean. Technol.* 30 (6):1123–1135. doi:[10.1175/JTECH-D-12-00168.1](https://doi.org/10.1175/JTECH-D-12-00168.1).
- DeCarlo, P. F., J. G. Slowik, D. R. Worsnop, P. Davidovits, and J. L. Jimenez. 2004. Particle morphology and density characterization by combined mobility and aerodynamic diameter measurements. Part 1: Theory. *Aerosol Sci. Technol.* 38 (12): 1185–1205. doi:[10.1080/027868290903907](https://doi.org/10.1080/027868290903907).
- Fan, J. W., Y. Wang, D. Rosenfeld, and X. H. Liu. 2016. Review of aerosol-cloud interactions: Mechanisms, significance, and challenges. *J. Atmos. Sci.* 73 (11): 4221–4252. doi:[10.1175/JAS-D-16-0037.1](https://doi.org/10.1175/JAS-D-16-0037.1).
- Flagan, R. C. 2011. Electrical mobility methods for submicrometer particle characterization. In *Aerosol measurement:*

- Principles, techniques, and applications*, eds. P. Kulkarni, P. A. Baron, and K. Willeke, 339–364. New York: John Wiley & Sons.
- Fults, S. L., A. K. Massmann, A. Montecinos, E. Andrews, D. E. Kingsmill, J. R. Minder, R. D. Garreaud, and J. R. Snider. 2019. Wintertime aerosol measurements during the Chilean coastal orographic precipitation experiment. *Atmos. Chem. Phys. Discuss.* (Forthcoming). doi: 10.5194/acp-2019-185
- Hermann, M., F. Stratmann, M. Wilck, and A. Wiedensohler. 2001. Sampling characteristics of an aircraft-borne aerosol inlet system. *J. Atmos. Ocean. Technol.* 18 (1):7–19. doi: 10.1175/1520-0426(2001)018<0007:SCOAB>2.0.CO;2.
- Hinds, W. C. 1982. *Aerosol technology. Properties, behavior, and measurement of airborne particles*. New York: John Wiley and Sons.
- Kulkarni, P., P. A. Baron, and K. Willeke (eds.). 2011. *Aerosol measurement: Principles, techniques, and applications*. New York: John Wiley and Sons.
- Kupc, A., C. Williamson, N. L. Wagner, M. Richardson, and C. A. Brock. 2018. Modification, calibration, and performance of the Ultra-High sensitivity aerosol spectrometer for particle size distribution and volatility measurements during the atmospheric tomography mission (ATom) airborne campaign. *Atmos. Meas. Tech.* 11(1):369–383. doi:10.5194/amt-11-369-2018.
- Malm, W. C. 2016. *Visibility: The seeing of near and distant landscape features*. Cambridge, MA: Elsevier Inc.
- McMurry, P. H. 2000. A review of atmospheric aerosol measurements. *Atmos. Environ.* 34 (12–14):1959–1999. doi:10.1016/S1352-2310(99)00455-0.
- Murphy, D. M., and M. E. Schein. 1998. Wind tunnel tests of a shrouded aircraft inlet. *Aerosol Sci. Technol.* 28 (1): 33–39. doi:10.1080/02786829808965510.
- Ortega, J., J. Smith, J. Snider, and J. Michael Reeves. 2019. Aerosol particle measurements taken during the airborn ARISTO 2016 campaign. (dataset). UC Irvine Dash data repository. Accessed May 3, 2019. <https://doi.org/10.7280/D1KD47>.
- Pfister, G. G., P. J. Reddy, M. C. Barth, F. F. Flocke, A. Fried, S. C. Herndon, B. C. Sive, J. T. Sullivan, A. M. Thompson, T. I. Yacovitch, A. J. Weinheimer, and A. Wisthaler. 2017. Using observations and Source-Specific model tracers to characterize pollutant transport during FRAPPE and DISCOVER-AQ. *J. Geophys. Res.-Atmospheres* 122 (19): 10474–10502. doi:10.1002/2017jd027257.
- Porter, J. N., A. D. Clarke, G. Ferry, and R. F. Pueschel. 1992. Aircraft studies of size-dependent aerosol sampling through inlets. *J. Geophys. Res.* 97 (D4):3815–3824. doi: 10.1029/91JD02886.
- Seinfeld, J., and S. Pandis. 1998. *Atmospheric chemistry and physics: From air pollution to climate change*. New York: John Wiley and Sons.
- Shah, S. D., and D. R. Cocker. 2005. A fast scanning mobility particle spectrometer for monitoring transient particle size distributions. *Aerosol Sci. Technol.* 39 (6):519–526. doi:10.1080/027868291004652.
- Sheridan, P. J., and R. B. Norton. 1998. Determination of the passing efficiency for aerosol chemical species through a typical aircraft-mounted, diffuser-type aerosol inlet system. *J. Geophysical Res.* 103 (D7):8215–8225. doi: 10.1029/98JD00286.
- Shiraiwa, M., K. Ueda, A. Pozzer, G. Lammel, C. J. Kampf, A. Fushimi, S. Enami, A. M. Arangio, J. Frohlich-Nowoisky, Y. Fujitani, A. Furuyama, P. S. J. Lakey, J. Lelieveld, K. Lucas, Y. Morino, U. Poschl, S. Takaharna, A. Takami, H. J. Tong, B. Weber, A. Yoshino, and K. Sato. 2017. Aerosol health effects from molecular to global scales. *Environ. Sci. Technol.* 51 (23):13545–13567. doi:10.1021/acs.est.7b04417.
- Stolzenburg, M. R., and P. H. McMurry. 1991. An ultrafine aerosol condensation nucleus counter. *Aerosol Sci. Technol.* 14 (1):48–65. doi:10.1080/02786829108959470.
- Takegawa, N., K. Iida, and H. Sakurai. 2017. Modification and laboratory evaluation of a TSI ultrafine condensation particle counter (model 3776) for airborne measurements. *Aerosol Sci. Technol.* 51 (2):235–245. doi:10.1080/02786826.2016.1261990.
- Toon, O. B., J. B. Pollack, and B. N. Khare. 1976. The optical constants of several atmospheric aerosol species: Ammonium sulfate, aluminum oxide, and sodium chloride. *J. Geophysical Res.* 81 (33):5733–5748. doi:10.1029/JC081i033p05733.
- Twohy, C. 1991. Airborne Condensation Nucleus Counter Users's Guide. NCAR Technical Note, NCAR/TN + 35EDD. Accessed December 11, 2018. <https://opensky.ucar.edu/islandora/object/technotes%3A124>
- UCAR/NCAR – Earth Observing Laboratory. 1994. NSF/NCAR Hercules C-130 Aircraft. Accessed December 11, 2018. <https://doi.org/10.5065/D6WM1BG0>.
- UCAR/NCAR – Earth Observing Laboratory. 2007. NSF/NCAR HIMIL inlet. Accessed December 11, 2018. <https://www.eol.ucar.edu/node/230>.
- UCAR/NCAR – Earth Observing Laboratory. 2005. NSF/NCAR GV HIAPER Aircraft. UCAR/NCAR – Earth Observing Laboratory. Accessed December 11, 2018. <https://doi.org/10.5065/D6DR2JP>.
- UCAR/NCAR – Earth Observing Laboratory. 2011. Air Sample Inlets for RAF Aircraft. Accessed December 11, 2018. <https://www.eol.ucar.edu/homes/dcrogers/Instruments/Inlets/>.
- Wang, S. C., and R. C. Flagan. 1990. Scanning electrical mobility spectrometer. *Aerosol Sci. Technol.* 13 (2): 230–240. doi:10.1080/02786829008959441.
- Wiedensohler, A. 1988. An approximation of the bipolar charge distribution for particles in the submicron size range. *J. Aerosol Sci.* 19(3):387–389. doi:10.1016/0021-8502(88)90278-9.
- Wilson, J. C., M. R. Stolzenburg, W. E. Clark, M. Loewenstein, G. V. Ferry, K. R. Chan, and K. K. Kelly. 1992. Stratospheric sulfate aerosol in and near the northern-hemisphere polar vortex – The morphology of the sulfate layer, multimodal size distributions, and the effect of denitrification. *J. Geophys. Res.* 97 (D8):7997–8013. doi:10.1029/92JD00065.
- Ye, C. X., X. L. Zhou, D. Pu, J. Stutz, J. Festa, M. Spolaor, C. Tsai, C. Cantrell, R. L. Mauldin, T. Campos, A. Weinheimer, R. S. Hornbrook, E. C. Apel, A. Guenther, L. Kaser, B. Yuan, T. Karl, J. Haggerty, S. Hall, K. Ullmann, J. N. Smith, J. Ortega, and C. Knote. 2016. Rapid cycling of reactive nitrogen in the marine boundary layer. *Nature* 532 (7600):489–491. doi:10.1038/nature17195.